



## Raman and Mössbauer spectroscopic studies of tungsten doped Ni–Zn nano ferrite

Pathania, A., Rana, K., Bhalla, N., Thakur, P., Estrela, P., Mattei, J. L., Queffelec, P., & Thakur, A. (2017). Raman and Mössbauer spectroscopic studies of tungsten doped Ni–Zn nano ferrite. *Journal of Materials Science: Materials in Electronics*, 28(1), 679-685. <https://doi.org/10.1007/s10854-016-5574-2>

[Link to publication record in Ulster University Research Portal](#)

### Published in:

Journal of Materials Science: Materials in Electronics

### Publication Status:

Published (in print/issue): 01/01/2017

### DOI:

[10.1007/s10854-016-5574-2](https://doi.org/10.1007/s10854-016-5574-2)

### Document Version

Author Accepted version

### General rights

Copyright for the publications made accessible via Ulster University's Research Portal is retained by the author(s) and / or other copyright owners and it is a condition of accessing these publications that users recognise and abide by the legal requirements associated with these rights.

### Take down policy

The Research Portal is Ulster University's institutional repository that provides access to Ulster's research outputs. Every effort has been made to ensure that content in the Research Portal does not infringe any person's rights, or applicable UK laws. If you discover content in the Research Portal that you believe breaches copyright or violates any law, please contact [pure-support@ulster.ac.uk](mailto:pure-support@ulster.ac.uk).

Click here to view linked References

## Raman and Mössbauer spectroscopic studies of tungsten doped Ni-Zn Nano ferrite

Abhilash Pathania<sup>1,2</sup>, Kush Rana<sup>2,3</sup>, Nikhil Bhalla<sup>4,5</sup>, Preeti Thakur<sup>2\*</sup>, Pedro Estrela<sup>5</sup>, Jean Luc  
Mattei<sup>6</sup>, Patrick Queffelec<sup>6</sup>, Atul Thakur<sup>2</sup>

<sup>1</sup>School of Mechanical and Civil Engineering, Shoolini University- Solan 173212, India

<sup>2</sup>Himalayan Centre of Excellence in Nanotechnology, Shoolini University- Solan 173212, India

<sup>3</sup>Nanotechnology Wing, Innovative Science Research Society, Shimla-171001, India

<sup>4</sup> Micro/Bio/Nanofluidics Unit Okinawa Institute of Science and Technology  
1919-1 Tancha, Onna-son, Kunigami-gun Okinawa, Japan 904-0495

<sup>5</sup>Departmentt of Electronic & Electrical Engineering, University of Bath, Bath BA2 7AY, United  
Kingdom

<sup>6</sup>Laboratoire des Sciences et Techniques, de l'Information, de la Communication et de la Connaissance,  
UMR CNRS 6285, 6 av. Le Gorgeu, CS 93837, 29238 BREST CEDEX 3, France

### **# Corresponding Author:**

\* Preeti Thakur

Himalayan Centre of Excellence in Nanotechnology

Shoolini University

Solan, H.P, INDIA

[at.preeti@gmail.com](mailto:at.preeti@gmail.com)

Phone: +91 1792 654049

## Abstract

In this study, tungsten substituted Ni-Zn nano ferrites of the composition  $\text{Ni}_{0.5}\text{Zn}_{0.5}\text{W}_x\text{Fe}_{2-x}\text{O}_4$  with  $x = 0.0, 0.2, 0.4$  have been synthesized by a co-precipitation method. The prepared samples were pre-sintered at  $850^\circ\text{C}$  and then annealed at  $1000^\circ\text{C}$  for 3 h each. The structural, morphological, optical and magnetic properties of these samples were studied by using X-ray diffraction (XRD), Field Emission Scanning Electron Microscopy (FE-SEM), Transmission Electron Microscopy (TEM), Fourier Transform Infrared Spectroscopy (FTIR), Raman spectroscopy (RS) and Mössbauer spectroscopy (MS). XRD revealed the formation of spinel single-phase structure with an average crystallite size of 53-60 nm. Fourier Transform Infrared Spectroscopy show two prominent peaks primarily due to the tetrahedral and octahedral stretching vibrations in the range of  $400\text{-}600\text{ cm}^{-1}$ . Raman spectra indicate first order three Raman active modes; ( $A_{1g} + E_g + T_{2g}$ ) at around 688, 475 and  $326\text{ cm}^{-1}$ . Mössbauer spectroscopy reveals that substitution of  $\text{W}^{3+}$  for  $\text{Fe}^{3+}$  cation results in reduction of total magnetic moment and consequently the net magnetization.

**Keywords:** Co-precipitation; Raman spectroscopy; Mössbauer spectroscopy.

## 1. Introduction

Ferrites are one of the most important materials on account of their remarkable electrical and magnetic properties. Ni–Zn ferrites are versatile soft ferrite materials investigated extensively due to their low dielectric losses and high resistivity [1]. Presently, these materials are largely studied at nanoscale to improve properties for diverse applications such as electromagnetic interference (EMI) suppression, gas sensing and biomedical systems [2-5]. The structural and magnetic properties of these ferrites are highly sensitive to the method of preparation, sintering parameters and the amount of metal oxides constituents. Nano ferrites can be prepared by methods such as citrate–gel methods, standard ceramic techniques, co-precipitation, polymeric assisted routes, hydrothermal methods, reverse micelles process, micro-emulsion methods and wet chemical methods [6-13]. Co-precipitation method is a simple and the most economical method to produce stoichiometric and uniform ferrites. In this technique, the mixing of metal ions takes place at atomic scale, which produces homogeneous material of nano crystallite size. Yu et. al (14) and Yang et al. (15) have successfully synthesized nano cubes of Co substituted  $\text{Fe}_2\text{O}_4$  with size ranging from 35-110 nm.

Tungsten oxide is a n-type semiconducting material, which finds potential applications in various technological fields due to its chemical composition and crystalline structure [16, 17]. Among transition metal oxides such as  $\text{WO}_3$  [18] and  $\text{NiO}$  [19] have attracted increasing attention as they exhibit morphological, optical and electronic properties suitable for organic optoelectronic devices. Indeed, the crystalline phase of  $\text{WO}_3$  plays a major role in catalysts [20] gas sensing [21] and hydrogen production [22]. Fu et. al. have studied the effect of tungsten on Ni-Zn ferrites. However, their investigation was limited to dielectric and magnetic study of  $\text{Ni}_{0.5}\text{Zn}_{0.5}\text{W}_x\text{Fe}_{2-x}\text{O}_4$  (where  $x = 0, 0.02, 0.04, 0.06, \text{ and } 0.08$ ) by one-step synthesis [23]. To the best of our knowledge,

no report is available on higher concentration doping of tungsten in Ni-Zn ferrites matrix and their spectroscopic analysis. Therefore, in the present work, structural and spectroscopic properties of high concentration tungsten doped Ni-Zn ferrites have been investigated.

## 2 Experimental

### 2.1. Synthesis of $\text{Ni}_{0.5}\text{Zn}_{0.5}\text{W}_x\text{Fe}_{2-x}\text{O}_4$

Tungsten substituted Ni – Zn ferrite series of composition  $\text{Ni}_{0.5}\text{Zn}_{0.5}\text{W}_x\text{Fe}_{2-x}\text{O}_4$  with  $x = 0.0, 0.2$  and  $0.4$  was prepared by a co-precipitation method. High purity chemicals: nickel chloride hexahydrate, zinc chloride, tungsten trioxide and iron (III) chloride hexahydrate were used in proper stoichiometric proportion and dissolved in the boiling solution of  $0.40\text{ M NaOH}$  under vigorous stirring for 40 minutes. Following this, the suspension was cooled to an ambient temperature and precipitate was washed carefully with distilled water several times to remove impurities. The mixture was then centrifuged and the residue was dried in an electrical oven at  $80^\circ\text{C}$  for overnight. The powders were pre-sintered at  $850^\circ\text{C}$  for 3h at a heating and cooling rate of  $200^\circ\text{C/h}$ . These powdered samples were pressed into pellets under a pressure of  $55\text{ MPa}$  using a uniaxial hydraulic press. These pellets were sintered at  $1000^\circ\text{C}$  for another 3 h at a heating and cooling rate of  $200^\circ\text{C/h}$  in a muffle furnace.

### 2.2 Characterization

X-ray diffraction (XRD) measurements were performed on an X-pert Pro Pan analytical diffractometer using  $\text{CuK}\alpha$  radiation. The Transmission Electron Microscopy (TEM) characterizations were carried out using  $80\text{ kV}$  Transmission electron microscope (Model -JEOL USA 2100F). Structural morphology of ferrite samples were examined by using MIRA3

TESCAN.FT-IR spectra were recorded using a Perkin Elmer spectrophotometer in the range 4000–400 cm<sup>-1</sup>. HORIBA JOBIN VYON LABRAM HR was used to study Raman spectra. Magnetic properties of these samples were studied by using WISSEL Mössbauer spectrometer. The evaluations of the Mössbauer spectra were performed by MOSWINN code.

### 3. Results and Discussion

Fig. 1 shows the XRD patterns of Ni<sub>0.5</sub>Zn<sub>0.5</sub>W<sub>x</sub>Fe<sub>2-x</sub>O<sub>4</sub> (x = 0.0, 0.2, 0.4) samples prepared by a co-precipitation method. The XRD patterns were found to possess well resolved, sharp and intense peaks corresponding to planes (220), (311), (222), (400), (422), (511) and (440) which indicated the presence of cubic spinel structure without the presence of any impurity. A single phase spinel structure was maintained with tungsten ion substitution inside the Ni-Zn ferrite matrix. This indicates that tungsten ions are properly dissolved in the lattice structure of Ni-Zn ferrite systems. The crystallite size of the main peak (311) is calculated by using the Scherrer's formula [24] and the values are listed in Table 1.

$$D = \frac{k\lambda}{\beta \cos \theta} \quad (1)$$

Where k is constant (shape factor 0.9),  $\lambda$  is the wave length of Cu (K $\alpha$ ) and  $\beta$  is the full width at half maxima. The XRD analysis showed that the crystallite sizes decrease uniformly from 60 nm to 53 nm with tungsten substitution from x = 0 to x = 0.4, respectively. The decrease in crystallite size is due to the smaller ionic radii of tungsten (0.55 Å) than Fe<sup>3+</sup> (0.63 Å). Lattice parameter 'a' was determined by using Bragg's law [25]. The calculated value for the lattice parameter is found to be 8.3730 Å at x = 0, which remains constant with increase in tungsten doping. The average lattice strain experienced by nanoferrites was calculated by using the Hall- Williamson plot using the formula [26],

$$LS = \frac{\beta \cos \theta}{4 \sin \theta} \quad (2)$$

where  $\beta$  is the full width at half maxima. All the plots show a negative slop which indicates that the compressive strain is experienced by the sintered samples, as shown in Fig. 2. This compressive strain is attributed to the variation of  $\text{Fe}^{3+}$  ions in the tetrahedral and octahedral sites due to grain size reduction. Another reason for such behavior of nanoscale ferrites may also be due to increased degree of inversion [27].

Figs.3 (a), (b) and (c) show the TEM image of  $\text{Ni}_{0.5}\text{Zn}_{0.5}\text{Fe}_2\text{O}_4$ . The image indicates that the particles are cubic in shape, narrowly distributed and agglomerated to some extent. This agglomeration can be due to the magnetic dipole interactions arising between ferrite particles [28]. The estimated average particle sizes are around 60 nm. This result agrees well with that estimated by XRD measurements.

Figs. 4(a), (b) and (c) illustrate the FESEM micrographs of nearly cubic shaped Ni-Zn ferrites nanoparticles with excellent homogenous crystalline structure. Furthermore, the ferrite powders are distributed regularly over the entire region showing fine grain growth with rare agglomeration due to the interactions of magnetic nanoparticles.

Fig. 5 shows the infrared spectra of the investigated ferrites in the range  $4000\text{--}400\text{ cm}^{-1}$ . There are only two main frequency bands ( $\nu_1$  &  $\nu_2$ ) that correspond to the intrinsic vibrations of tetrahedral and octahedral  $\text{Fe}^{3+}\text{--O}^{2-}$  complexes, respectively, and are typical characteristic of ferrites. The values of absorption band frequency is given in Table 1. The absorption band at  $592\text{ cm}^{-1}$  was assigned to tetrahedral sites where intrinsic stretching vibrations of the metal were observed. Whereas the band observed at  $423\text{ cm}^{-1}$  were assigned to octahedral-metal stretching corresponding to bond-bending vibrations [29]. The increasing values of  $\nu_1$  show that the normal mode of vibration of the tetrahedral cluster is more than that of the octahedral cluster. This

indicates that the tetrahedral cluster has a shorter bond length than that of the octahedral cluster [30]. The band  $\nu_1$  is attributed to the stretching vibration of  $\text{Fe}^{3+} - \text{O}^{2-}$  in tetrahedral site and the  $\nu_2$  to that of octahedral site. The position and intensity of  $\nu_1$  and  $\nu_2$  remain same with tungsten ions doping indicating all the tungsten ions are properly absorbed in the cubic lattice

Raman spectroscopy provides the structural properties of materials and to identify the microscopic vibrations caused by the slight structure distortion. Raman vibrational modes for tetrahedral and octahedral sites are tabulated in Table 2. Fig. 6 shows that all samples have more than five Raman active modes predicted by group theory in the normal spinel structure. The three major peaks ( $A_{1g} + E_g + T_{2g}$ ) at around 688, 475 and 326  $\text{cm}^{-1}$  which is approximately similar to the results obtained by Zhang et al. [31]. The mode  $A_{1g}$  ( $\sim 690 \text{ cm}^{-1}$ ) is due to symmetric stretching of oxygen atoms along Fe–O bonds [32, 33]. The mode  $E_g$  ( $\sim 320 \text{ cm}^{-1}$ ) is due to symmetric bending of oxygen with Fe and the mode  $T_{2g}$  (3) ( $\sim 546 \text{ cm}^{-1}$ ) is due to asymmetric bending of Fe (Ni)-O bonds.  $T_{2g}$  (1) ( $\sim 205 \text{ cm}^{-1}$ ) is due to translational motion of the whole tetrahedron. Raman modes at  $T_{2g}$  (1) and  $T_{2g}$  (2) are absent. The absence of these modes may be attributed to the cation inversion and also due to the effect of small crystallites, which leads to the broadening of modes. The broad shoulders below  $A_{1g}$  and  $T_{2g}$  (2) peaks were fitted with secondary bands at  $\sim 635 \text{ cm}^{-1}$  and  $\sim 435 \text{ cm}^{-1}$ , respectively. One peak corresponds to the unit cell with all Fe ions and the other one to the unit cell with mixed Fe and Ni ions. These secondary bands at low energy side are attributed to second overtone of  $A_{1g}$  and  $T_{2g}$  (2) modes and indicate inverse spinel structure [34].

Mossbauer spectroscopy is vastly sensitive to small variations in electron density at the iron nucleus, due to different electronic and structural environments. Fig. 7 shows Mössbauer spectra of all the powder samples annealed at temperature of 1000°C. Mössbauer spectroscopy gives quantitative information on “hyperfine interactions” which are small energies from the



interaction between the nucleus and its neighboring electrons. The area under the Mossbauer sub spectrum were used to calculate percent site occupancy of ions and actual chemical composition of tungsten doped Ni-Zn ferrite. Line-widths and area were considered for the B site because of the distribution of sextets on B-site. The best fit could be obtained by employing two sextets (A) and (B) in the Mössbauer Spectra indicating the distribution of interatomic spacing and distributed local environment of Fe cation. The sextet A was attributed to tetrahedral site while sextet B towards octahedral site [35]. It is well known that each A-site ion has 12 B-site neighbors in its immediate surroundings and each B-site ion has 6 A-site nearest neighbors.  $\text{Fe}^{3+}(\text{A})-\text{O}_2-\text{Fe}^{3+}(\text{B})$  exchange interaction between iron ions is known to be the strongest, whereas A–A and B–B interactions between iron ions via oxygen ions are relatively weaker. The line width of the  $^{57}\text{Fe}$  Mössbauer spectra is useful for the estimation of cation disorder effects on both magnetic and electric interactions. According to the Mössbauer spectra, the fractional area of the tetrahedral sites was decreased from 40 to 35 and the fractional area of octahedral site were increased from 60 to 65 with the doping of tungsten elements. This site preference occupancy confirmed the reduction of  $\text{Fe}^{3+}$  cation in octahedral site and it is concluded that the tungsten ions preferred to occupy the octahedral site. The tungsten elements are categorized in paramagnetic state and have down spin configuration, in spite of the fact that  $\text{Fe}^{3+}$  cations have ferromagnetic characteristics, and also have up spin configuration. However, the substitution of  $\text{Fe}^{3+}$  cation by  $\text{W}^{3+}$  cations results in reduction of total magnetic moment. Consequently, the magnetization in octahedral site was decreased. The line width of tetrahedral site is decreasing and increasing in octahedral site with increase in tungsten concentration. This may be attributed to the change of  $\text{Fe}^{3+}$  ions at A and B sites. The spectral parameters such as isomer shift ( $\delta$ ), quadrupole splitting (QS) and hyperfine field ( $H_{\text{eff}}$ ) are computed and tabulated in Table 3. The  $\text{Fe}^{3+}$  ions present in A and B site are expected to

experience a distribution in the magnetic hyperfine field due to different numbers nonmagnetic ( $\text{Zn}^{2+}$ ) and magnetic ( $\text{Ni}^{2+}$ ) neighbors and different degrees of collective magnetic excitation for the samples having wide particle size distributions. The isomer shift provides changes occurred in the chemical environment of the spinel lattice due to substitution of tungsten. But the observed changes in the isomer shift values with the substitution of tungsten ions appear to be very small. This infers that tungsten ions would not disturb the chemical environment around each A and each B- sub lattice in the spinel lattice. Hence, no appreciable change in the isomer shift has been noticed.

## Conclusion

Tungsten doped Ni-Zn nano-ferrites  $\text{Ni}_{0.5}\text{Zn}_{0.5}\text{W}_x\text{Fe}_{2-x}\text{O}_4$  with  $x=0, 0.2, \& 0.4$  are synthesized by co-precipitation method. The crystallite size of the samples decreases from 60 nm to 53 nm with increase in tungsten ions doping. This is because the ionic radius of tungsten (0.55 Å) is less than  $\text{Fe}^{3+}$  (0.63 Å). The calculated value for the lattice parameter is found to be 8.3730 Å at  $x=0$ , which is almost maintained with increase in tungsten doping. The lattice strain of the sintered powder shows the negative slop which indicates compressive strain in all the samples. TEM images show agglomeration to some extent with particle size around 60 nm. SEM micrographs show homogenous crystalline structure. FT-IR technique was used to locate the band position of the intrinsic vibrations of tetrahedral and octahedral groups respectively. FT-IR spectra were recorded in the range 4000–400  $\text{cm}^{-1}$ . There is no change in frequency bands ( $\nu_1$ ) and ( $\nu_2$ ) with tungsten doping indicating that these ions are properly absorbed in the cubic lattice. Raman spectroscopy provides the microscopic vibrations caused by the slight structure distortion. The Mössbauer spectra reveals that all the samples show broadened six line patterns and exhibits a hysteretic behavior, indicating that it has ferromagnetic phase.

1  
2  
3  
4  
5  
6  
7  
8  
9 **Acknowledgment:**

10  
11  
12 Authors are grateful to the Department of Science and Technology (DST), Government of  
13 India, for the financial support vide sanction no SERB/F/7451/2013-14. Authors are also  
14  
15 thankful to Prof. Mahavir Singh and his team for helping us in Mössbauer characterization.  
16  
17  
18  
19  
20  
21  
22  
23  
24  
25  
26  
27  
28  
29  
30  
31  
32  
33  
34  
35  
36  
37  
38  
39  
40  
41  
42  
43  
44  
45  
46  
47  
48  
49  
50  
51  
52  
53  
54  
55  
56  
57  
58  
59  
60  
61  
62  
63  
64  
65

## References:

1. Atul Thakur, Preeti Thakur, Jen-Hwa Hsu, J. Appl. Phys. 111, 07A305(2012)
2. D. Stoppels, J. Magn. Magn. Mater. 160 323–328, (1996)
3. K.H. Lee, D.H. Cho, S.S. Jeung, J. Mater. Sci. Lett. 16 83–87(1997).
4. T.J. Shinde, A.B. Gadkari, P.N. Vasambekar, J. Magn. Magn. Mater. 333 152–155(2013).
5. T. Feczko, A. Muskotal, L. Gal, J. Szepvolgyi, A. Sebestien, F. Vondervise, J. Nano Res. 10 227–232(2008).
6. Kush Rana, Preeti Thakur, Parul Sharma, M. Tomar, V. Gupta, Atul Thakur, Ceram. Int. 41 4492–4497(2015)
7. Atul Thakur, Preeti Mathur, M. Singh, Ind. J Pure App. Phys. 46, 42-46(2008).
8. A. Thakur, P. Thakur, J-H. Hsu, Scripta Mater. 64, 205-208(2011)
9. M. Mozaffari, J. Amighian, J. Magn. Magn. Mater. 260, 244-249, (2003).
10. Atul Thakur, Parul Sharma. Preeti Thakur, Int. J. Mod. Phys. B, 29, 1550183-1550196 (2015).
11. M. Hashim, Alimuddin, S. Kumar, B.H. Koo, S.E. Shirsath, E.M. Mohammed, J. Shah, R.K. Kotnala, H.K. Choi, H. Chung, R. Kumar, J. Alloy. Compd. 518, 11–18 (2012).
12. M.J. Iqbal, S. Farooq, Mater. Sci. Eng. B 136, 140–147, (2007).
13. Ashish Saini, Kush Rana, Atul Thakur, Preeti Thakur, Jean Luc Mattei, Patrick Queffelec, Mater. Res. Bull. 76 (2016) 94–99
14. Y. Yu, A. Mendoza-Garcia, B. Ning, S. Sun, Advanced Materials 25(2013) 3090-3094
15. W. Yang, Y. Yu, L. Wang, C. Yang, H. Li, Nanoscale 7 (2015) 2877-2882.
16. W. Kim, J.K. Kim, Y. Lim, I. Park, Y.S. Choi, J.H. Park, Sol. Energy Mater. Sol. Cells 122, 24–30, (2014).

17. M. Vasilopoulou, D. Davazoglou, Mater. Sci. Semicond. 16, 1196–1216, (2013).
18. N. Li, T. Stubhan, N.A. Luechinger, S.C. Halim, G.J. Matt, T. Ameri, C.J. Brabec, Org. Electron. 13, 2479–2484 (2012).
19. T. Ripolles-Sanchis, A. Guerrero, E. Azaceta, R. Tena-Zaera, G. Garcia-Belmonte, Sol. Energy Mater. Sol. Cells 117, 564–568 (2013).
20. D.B. Hernandez-Uresti, D. Sánchez-Martínez, A. Martínez-de la Cruz, S. Sepúlveda-Guzmán, L.M. Torres-Martínez, Ceram. Int. 40, 9–22 (2013).
21. N. Datta, N. Ramgir, M. Kaur, M. Roy, R. Bhatt, S. Kailasaganapathi, A.K. Debnath, D.K. Aswal, S.K. Gupta, Mater. Chem. Phys. 134, 851–857 (2012).
22. N. Naseri, H. Kim, W. Choi, A.Z. Moshfegh, Int. J. Hydrog. Energy 38, 2117–2125 (2013).
23. Xiuli Fu, Huilin Ge, Qingkai Xing, Zhijian Peng, Mater. Sci and Engg. B, 176, 926–931 (2011).
24. S. S. Thakur, A. Pathania, P. Thakur, A. Thakur, J-H. Hsu, Ceram Int. 41, 5072–5078, (2015).
25. M.A. Gabal, R. E. M. El-Shishtawy, Y.M. Al Angari, J. Magn. Mater. 324, 2258 – 2264 (2012).
26. A. Pathania, P. Thakur, A. Sharma, J.H. Hsu, A. Thakur, Ceram Int. 41, 10803–10809 (2015).
27. A. Thakur, P. Thakur, J-H. Hsu, Z. Phys. Chem.; 228 (6-7); 663–672 (2014)
28. Atul Thakur, Preeti Thakur, Jen-Hwa Hsu, IEEE Trans. Mag. 47, 4336–4339 (2011)
29. R. Islam, M.A. Hakim, H.N. Das, M.A. Mamun, J. Alloy. Compd. 559, 174–180, (2013).
30. S.A. Mazen, S.F. Mansour, E. Dhahri, H.M. Zaki, T.A. Elmosalami, J. Alloys Compd. 470, 294–300 (2009).

- 1  
2  
3  
4 31. S.S. Kumbhar, M.A. Mahadik, V. S. Mohite, Y.M. Hunge, K.Y. Rajpure, C. H.  
5  
6 Bhosale, Mater. Res. Bull. 67, 47-54(2015).  
7  
8  
9 32. G Rana, U. C. Johri, J. Alloys Compd. 577, 376–381(2013).  
10  
11 33. Z.W. Wang, P. Lazor, S.K. Saxena, G. Airtoli, J. Solid State Chem. 165, 165-170(2002).  
12  
13 34. A. Ahlawat, V.G. Sathe, V.R. Reddy, A. Gupta, J. Magn. Magn. Mater. 323, 2049-  
14  
15 2054(2011).  
16  
17  
18 35. S. Singhal, S. K. Barthwal, K. Chandra, J. Magn. Magn. Mater. 296, 94–103(2006).  
19  
20  
21  
22  
23  
24  
25  
26  
27  
28  
29  
30  
31  
32  
33  
34  
35  
36  
37  
38  
39  
40  
41  
42  
43  
44  
45  
46  
47  
48  
49  
50  
51  
52  
53  
54  
55  
56  
57  
58  
59  
60  
61  
62  
63  
64  
65

## Fig. Captions

Fig. 1. X-ray diffraction patterns of  $\text{Ni}_{0.5}\text{Zn}_{0.5}\text{W}_x\text{Fe}_{2-x}\text{O}_4$  ( $x = 0, 0.2, 0.4$ )

Fig. 2. Hall- Williamson Plots for  $\text{Ni}_{0.5}\text{Zn}_{0.5}\text{W}_x\text{Fe}_{2-x}\text{O}_4$  ( $x = 0, 0.2, 0.4$ )

Fig. 3. TEM images for  $\text{Ni}_{0.5}\text{Zn}_{0.5}\text{W}_x\text{Fe}_{2-x}\text{O}_4$  ( $x = 0, 0.2, 0.4$ )

Fig. 4. FESEM images for  $\text{Ni}_{0.5}\text{Zn}_{0.5}\text{W}_x\text{Fe}_{2-x}\text{O}_4$  ( $x = 0, 0.2, 0.4$ )

Fig. 5. FTIR spectra of  $\text{Ni}_{0.5}\text{Zn}_{0.5}\text{W}_x\text{Fe}_{2-x}\text{O}_4$  ( $x = 0, 0.2, 0.4$ )

Fig. 6. Raman spectra of  $\text{Ni}_{0.5}\text{Zn}_{0.5}\text{W}_x\text{Fe}_{2-x}\text{O}_4$  ( $x = 0, 0.2, 0.4$ )

Fig. 7. Mössbauer spectra of  $\text{Ni}_{0.5}\text{Zn}_{0.5}\text{W}_x\text{Fe}_{2-x}\text{O}_4$  ( $x = 0, 0.2, 0.4$ )

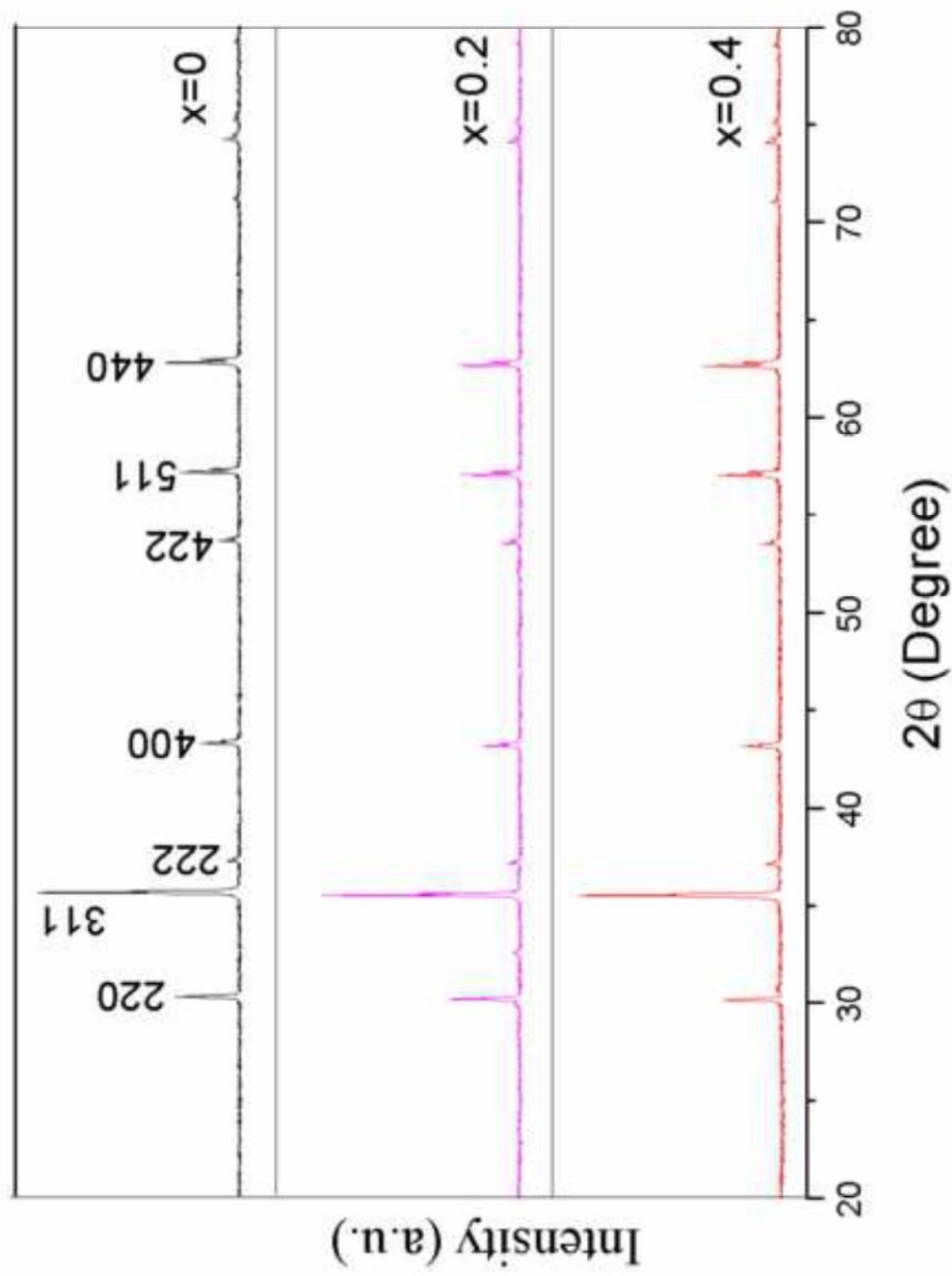
**List of Tables:**

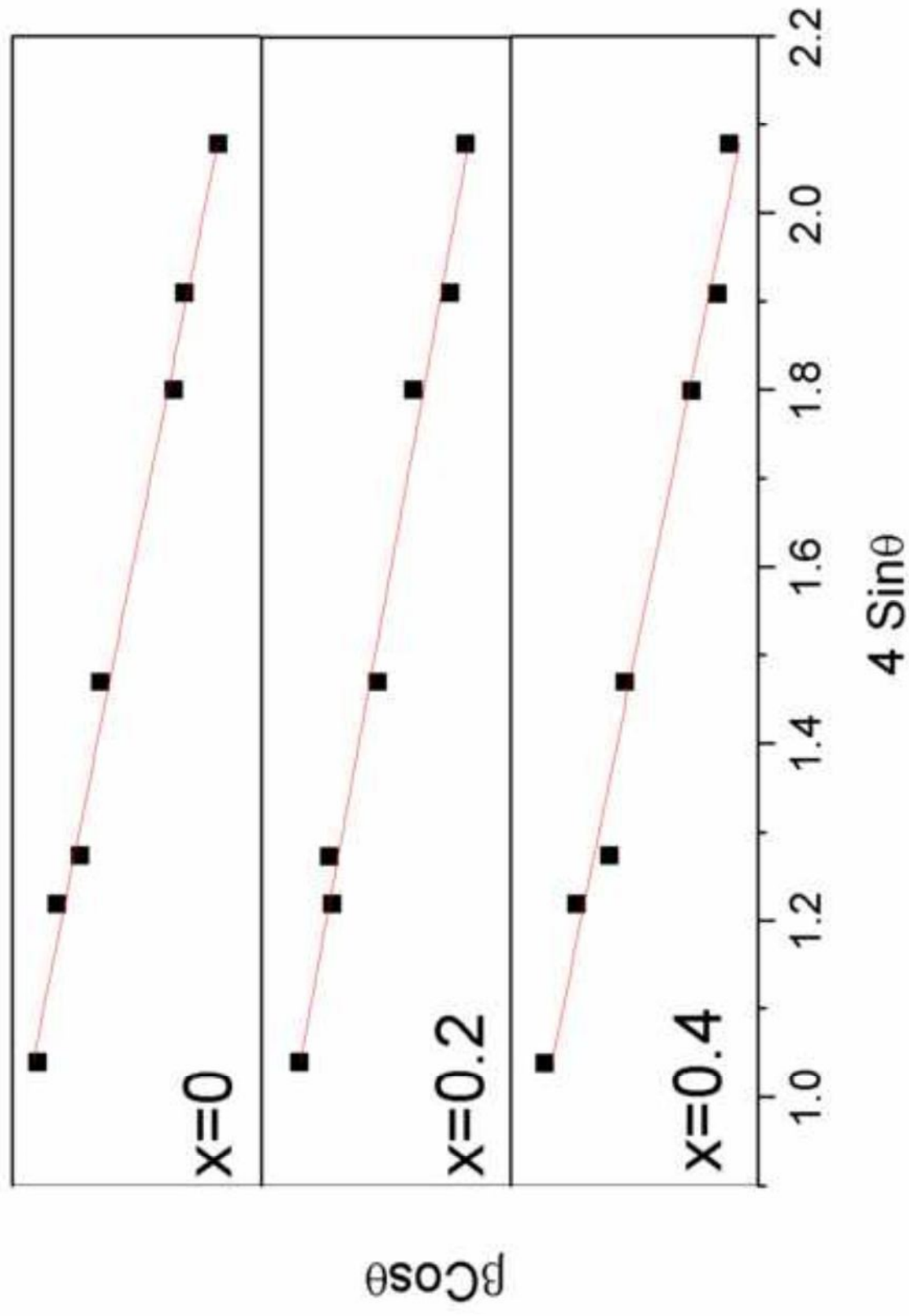
Table 1 Observed values of crystallite Size, theoretical densities experimental densities Porosity, Lattice strain, Lattice Constant & FT-IR spectral data.

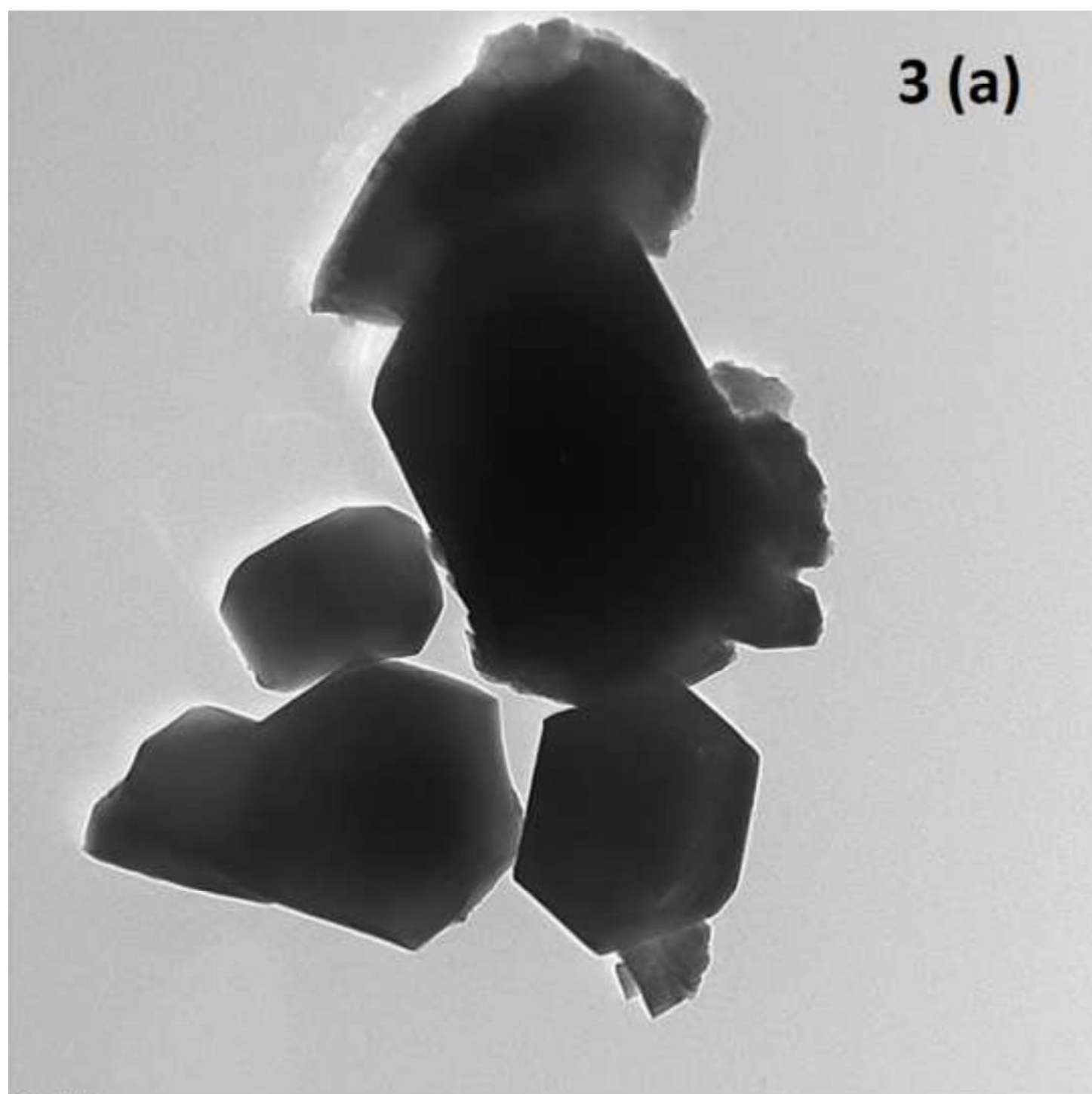
Table: 2 Raman Vibrational modes for tetrahedral and octahedral sites for  $\text{Ni}_{0.5}\text{Zn}_{0.5}\text{W}_x\text{Fe}_{2-x}\text{O}_4$  ( $x=0, 0.2, 0.4$ )

Table 3 Isomer shift ( $\delta$ ), quadrupole splitting (QS) and hyperfine field ( $H_{\text{eff}}$ ), line width for the two sextets of the system  $\text{Ni}_{0.5}\text{Zn}_{0.5}\text{W}_x\text{Fe}_{2-x}\text{O}_4$ .









AB5.tif

Print Mag: 174000x @ 7.0 in

3:33:24 p 10/06/15

---

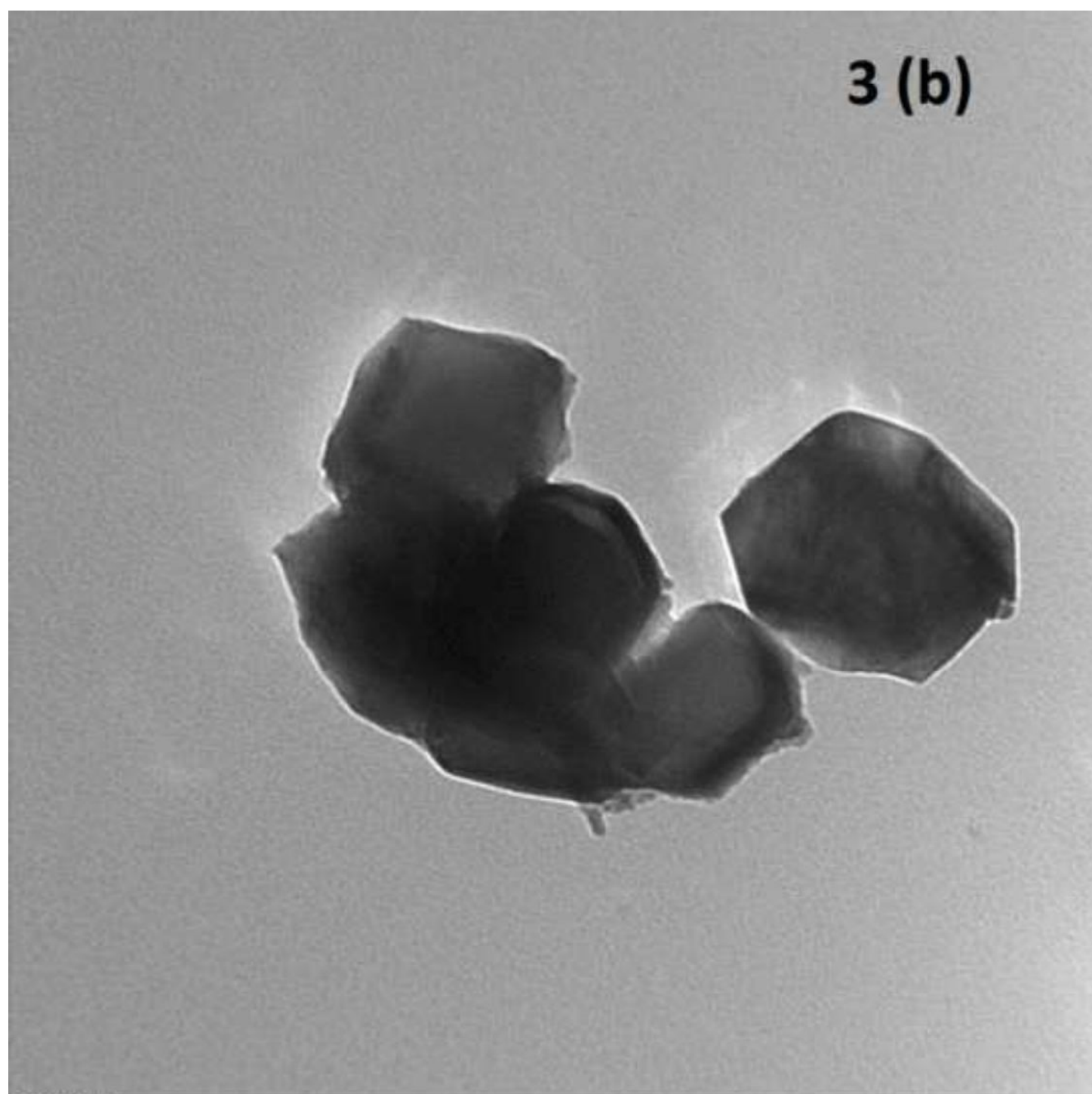
100 nm

HV=100.0kV

Direct Mag: 100000x

AMT Camera System





ABFJ.tif

Print Mag: 347000x @ 7.0 in

3:38:51 p 10/06/15

---

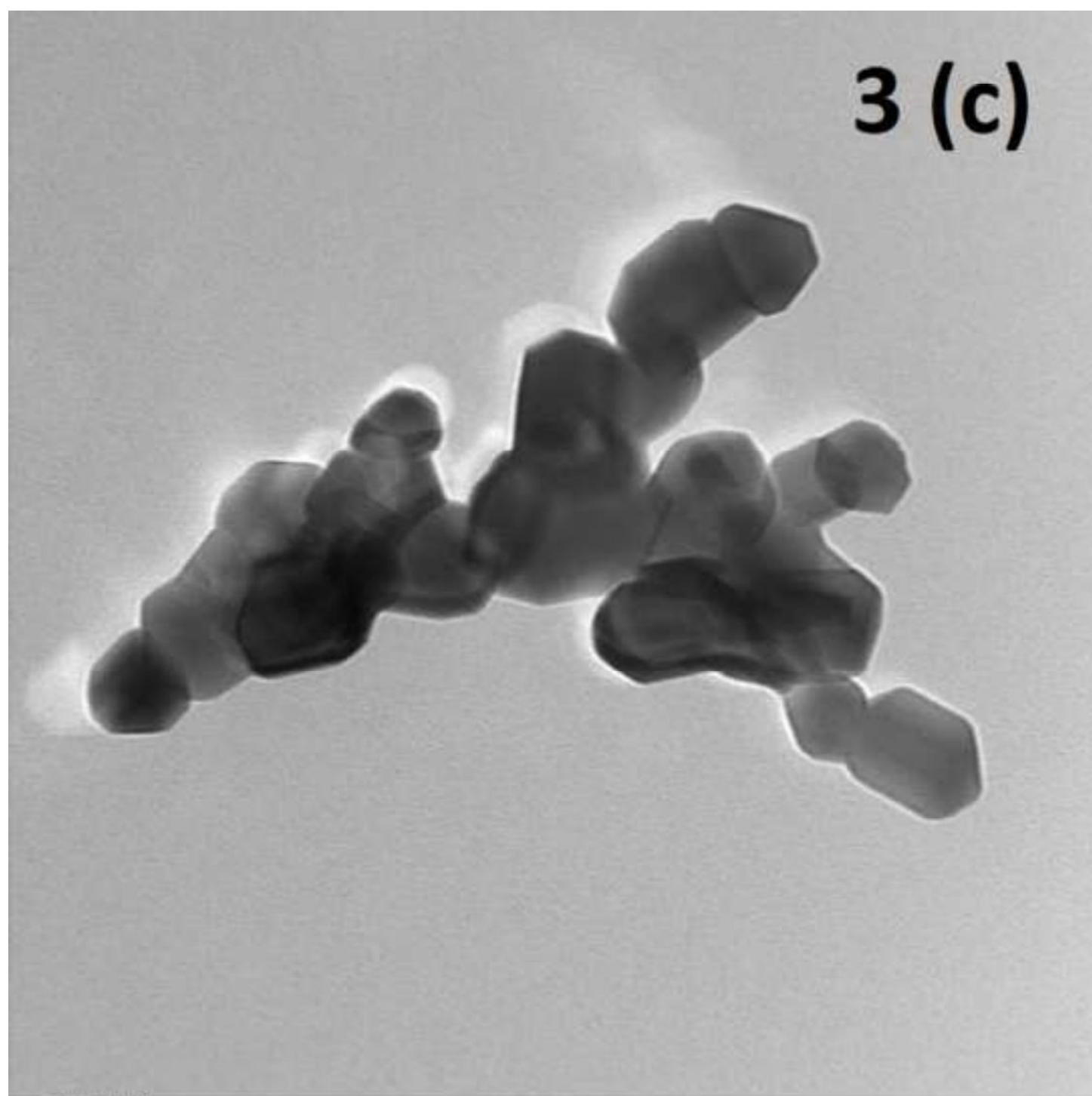
100 nm

HV=100.0kV

Direct Mag: 200000x

AMT Camera System





sm 0bv.h.tif

Print Mag: 347000x @ 7.0 in

3:12:25 p 10/06/15

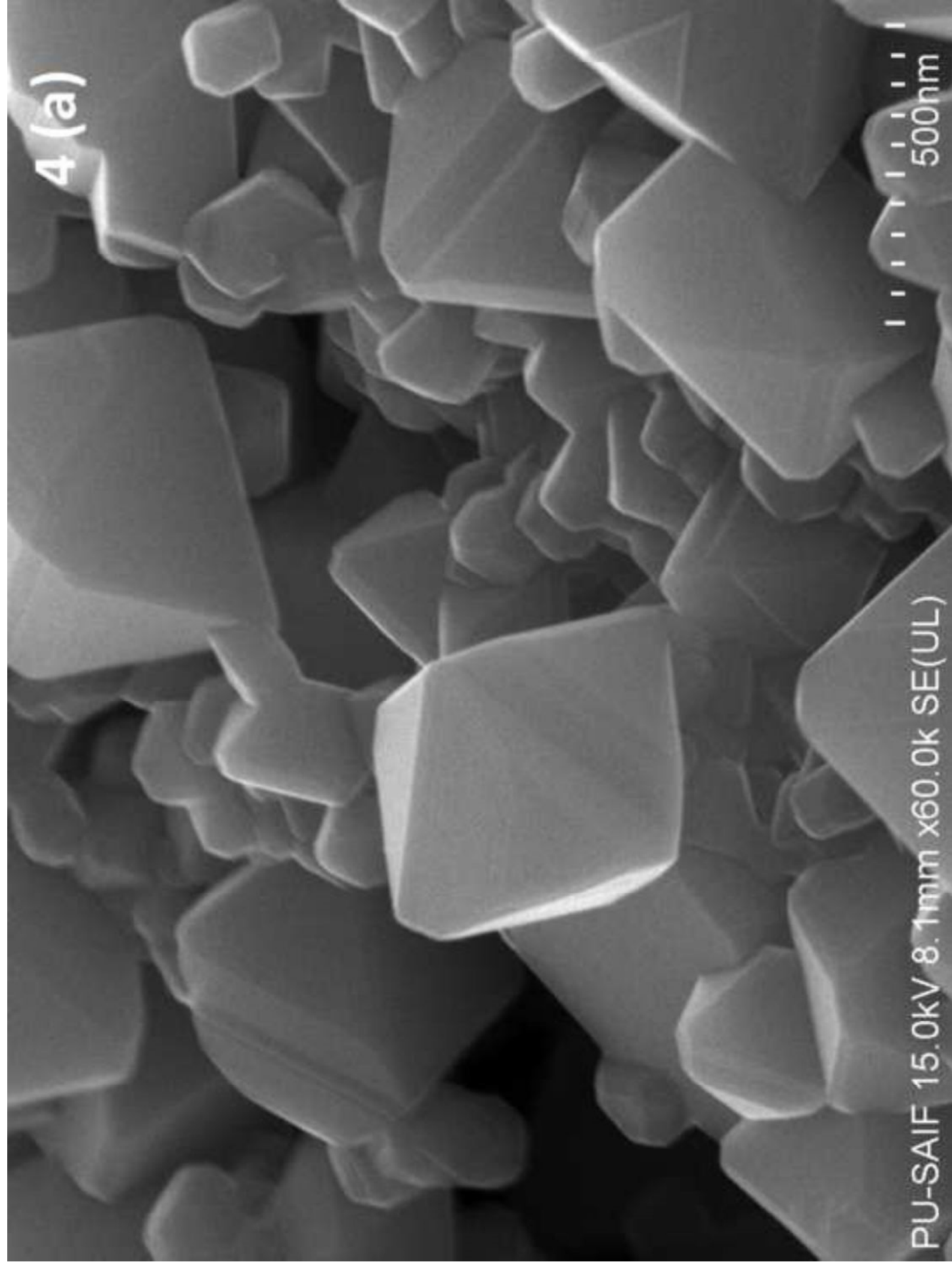
100 nm

HV=100.0kV

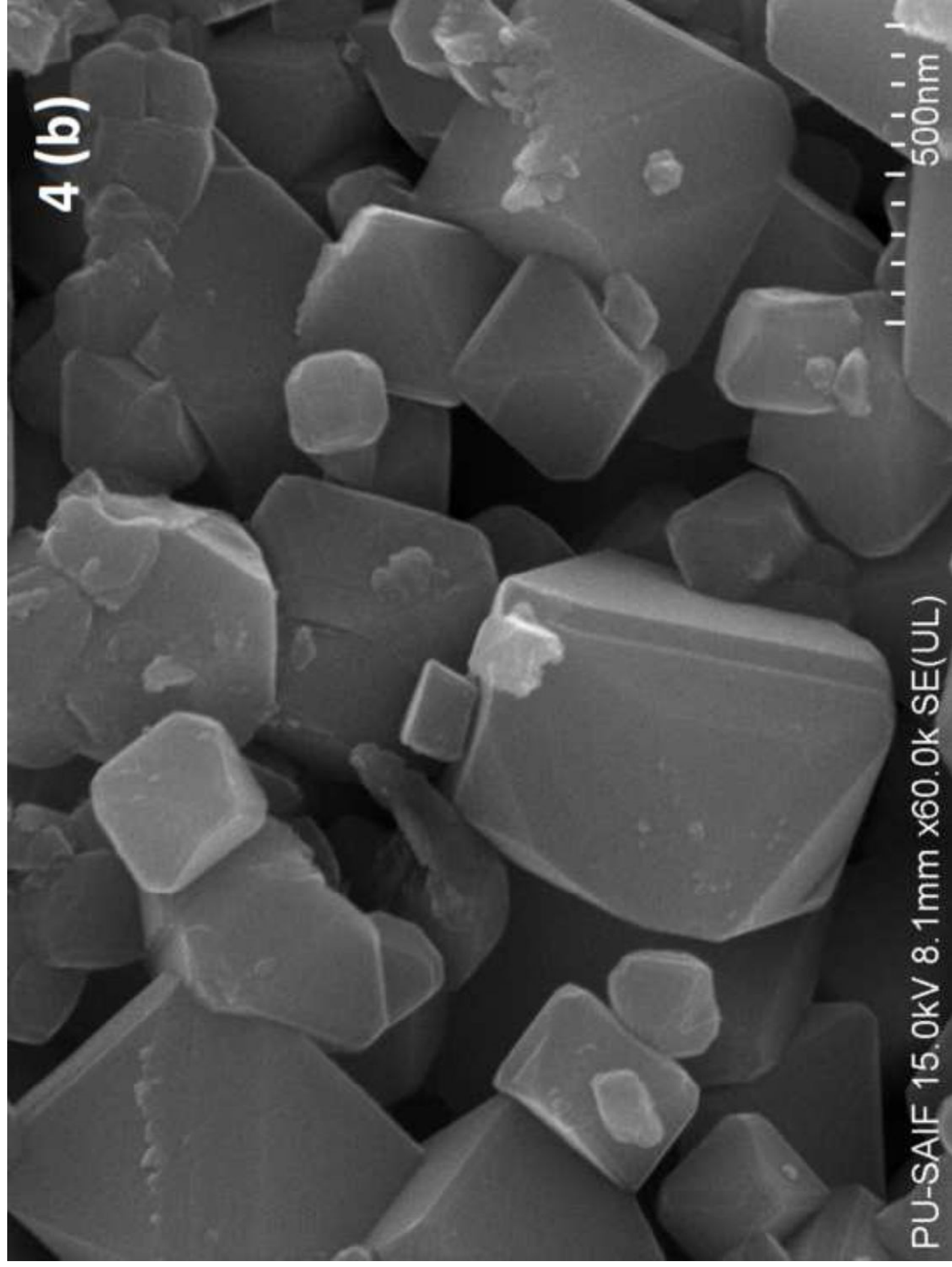
Direct Mag: 200000x

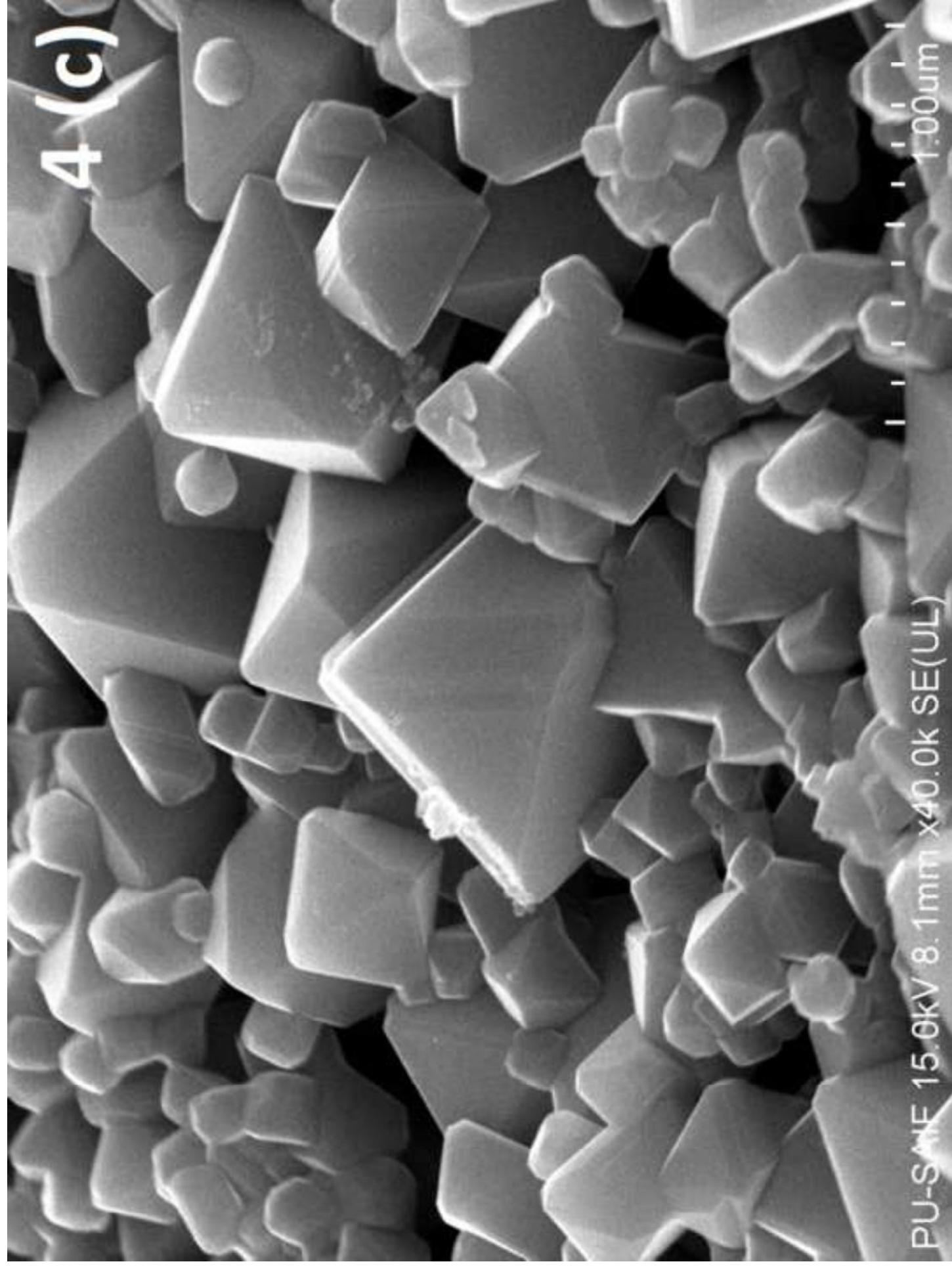
AMT Camera System



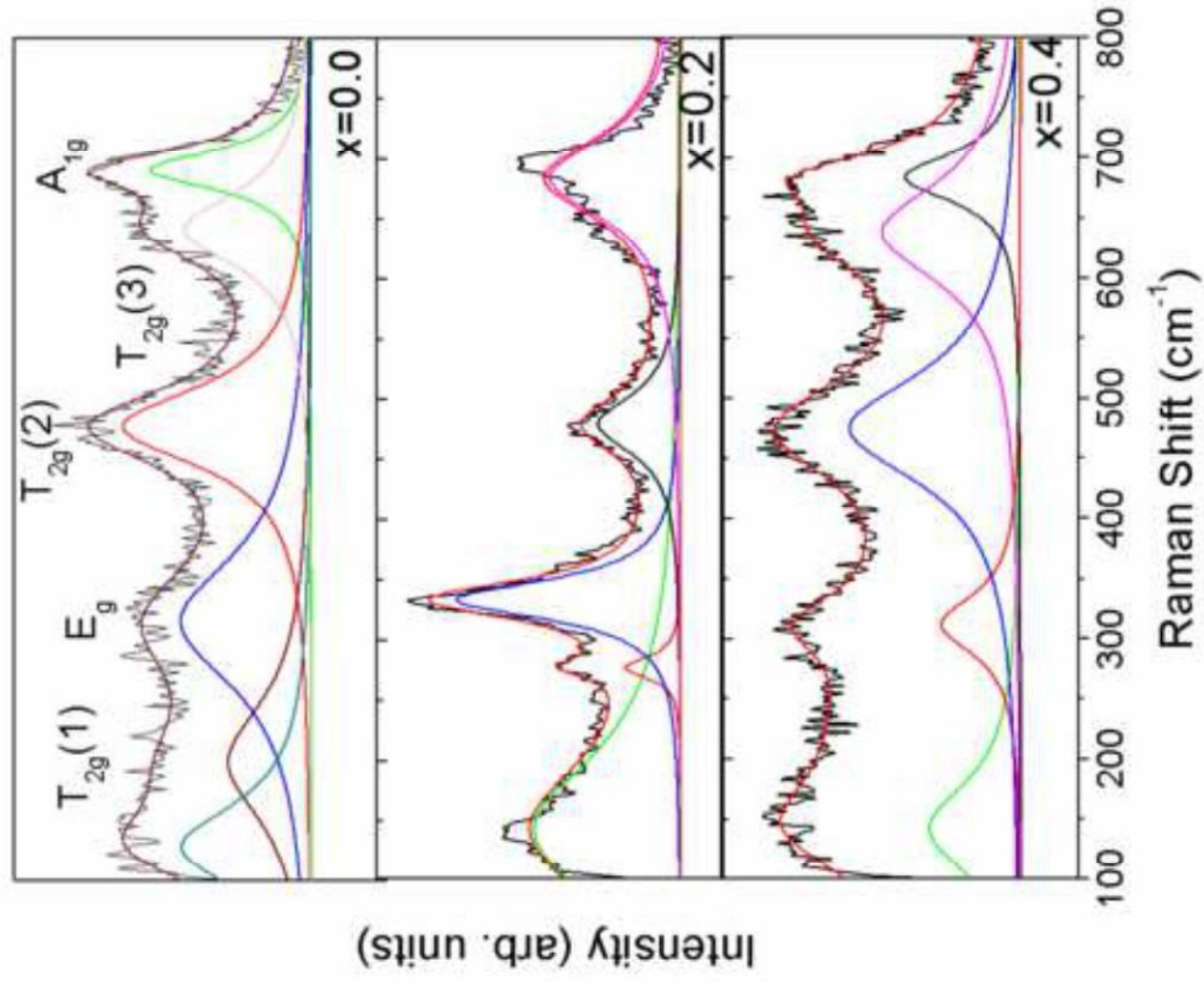


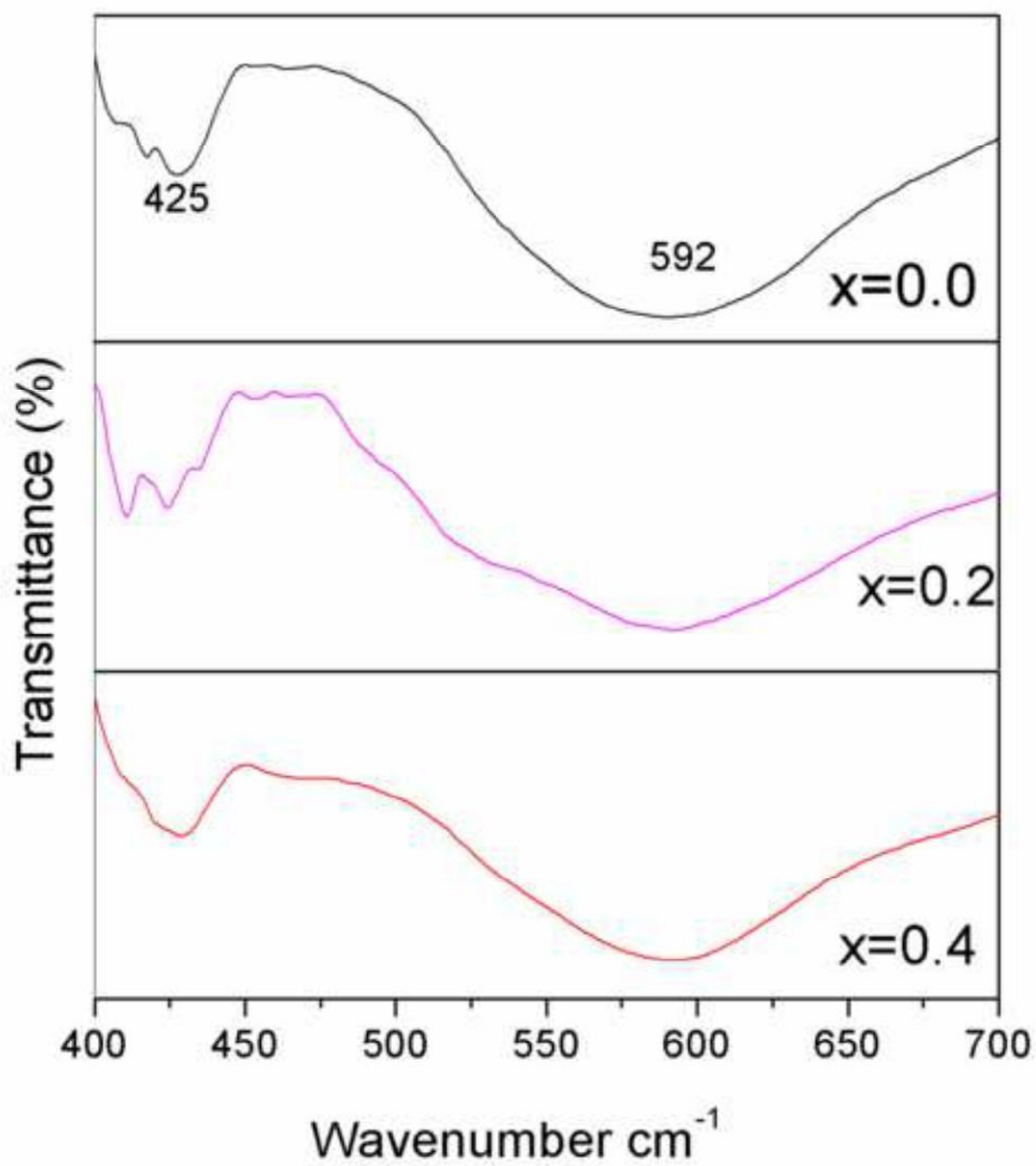












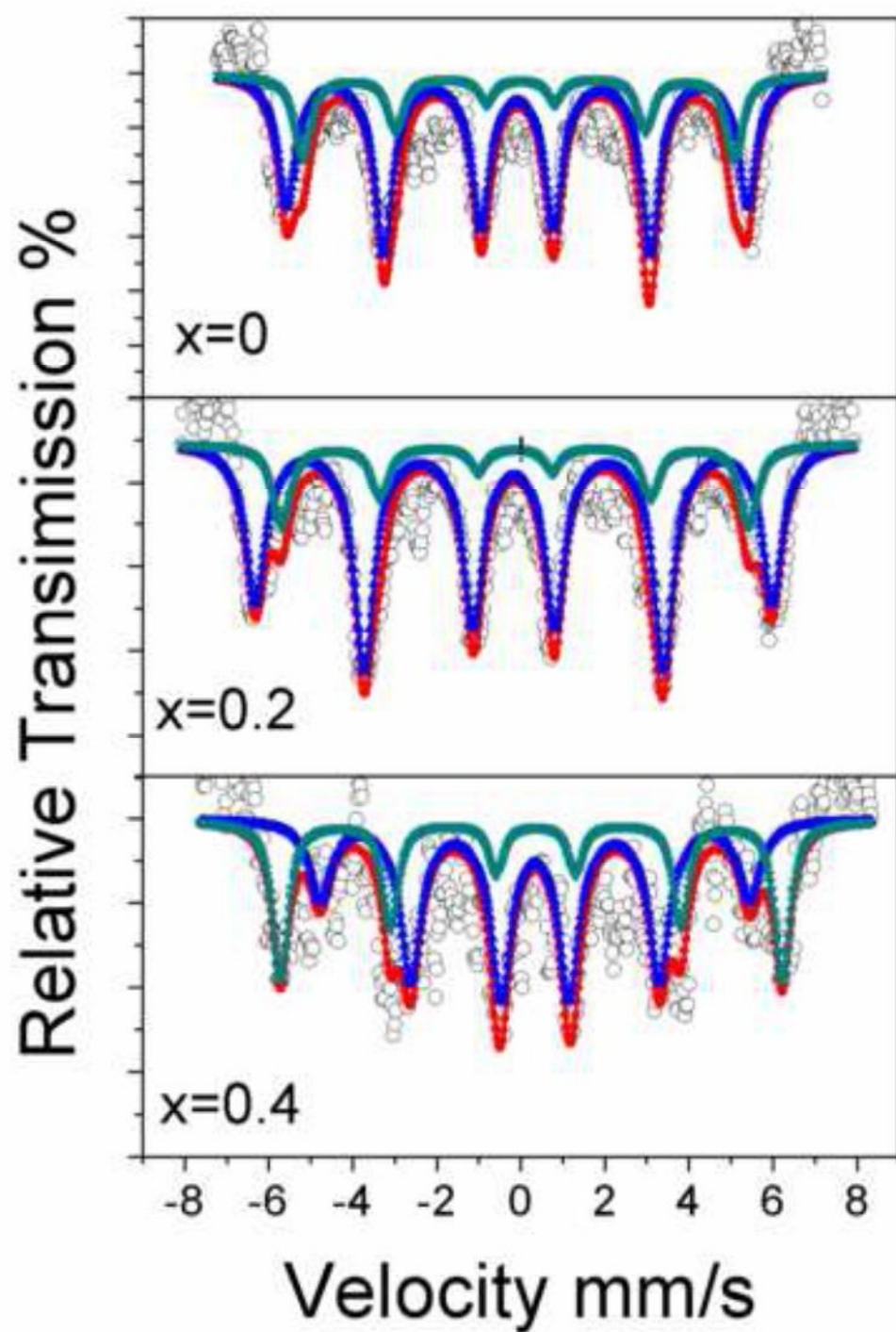


**Table 1**

Observed values of crystallite Size, Lattice strain, Lattice Constant & FT-IR spectral data.

Sample	D (nm)	LSx10 <sup>-3</sup>	a (Å)	$\nu_1$ (cm <sup>-1</sup> )	$\nu_2$ (cm <sup>-1</sup> )
X = 00	60	-7.90	8.3730	592	423
X = 0.2	57	-9.84	8.3732	592	424
X = 0.4	53	-1.61	8.3735	592	425

**Table: 2**

Raman Vibrational modes for tetrahedral and octahedral sites for  $\text{Ni}_{0.5}\text{Zn}_{0.5}\text{W}_x\text{Fe}_{2-x}\text{O}_4$  ( $x = 0, 0.2, 0.4$ )

Composition (x)	Raman Shift ( $\text{cm}^{-1}$ )				
	$A_{1g}$	$E_g$	$T_g(3)$	$T_g(2)$	$T_g(1)$
0.0	690	330	543	475	219
0.2	693	331	550	469	214
0.4	682	312	542	472	215

**Table 3**

Isomer shift ( $\delta$ ), quadrupole splitting (QS) and hyperfine field ( $H_{\text{eff}}$ ), line width for the two sextets of the system  $\text{Ni}_{0.5}\text{Zn}_{0.5}\text{W}_x\text{Fe}_{2-x}\text{O}_4$ . ( $x = 0, 0.2, 0.4$ )

Sample	SextetA (Tetrahedral site)					SextetB (Octahedral site)				
	WID	$\delta$	Q.S.	$H_{\text{eff}}$	Area	WID	$\delta$	Q.S.	$H_{\text{eff}}$	Area
	(mm/s)	(mm/s)	(mm/s)	(kOe)	(%)	(mm/s)	(mm /s)	(mm/s)	(kOe)	(%)
$\text{Ni}_{0.5}\text{Zn}_{0.5}\text{Fe}_2\text{O}_4$	0.58	0.27	-0.67	44.31	40	0.63	0.30	0.26	47.89	60
$\text{Ni}_{0.5}\text{Zn}_{0.5}\text{W}_{0.2}\text{Fe}_{1.8}\text{O}_4$	0.56	0.28	-0.30	44.73	37	0.68	0.25	0.31	47.66	63
$\text{Ni}_{0.5}\text{Zn}_{0.5}\text{W}_{0.4}\text{Fe}_{1.6}\text{O}_4$	0.56	0.23	-0.38	45.60	35	0.70	0.30	0.56	47.08	65